

Electrochemical-thermal coupled model for the optimal design of a liquid cooling module of a cylindrical lithium-ion battery

Huanhuan Li^{1,3}, Yijie Wang¹, Zhengjian Gu⁴, Yaping Wang^{2,3,*}, Chaofeng Pan¹, Long Chen¹,
Haobin Jiang¹

¹ Automotive Engineering Research Institute, Jiangsu University, 301 Xuefu Road, Zhenjiang 212013, P. R. China

² School of Materials Science & Engineering, Jiangsu University, Zhenjiang 212013, P. R. China

³ Key Laboratory of Advanced Energy Materials Chemistry (Ministry of Education), College of Chemistry, Nankai University, 94 Weijing Road, Tianjin, 300071, PR China

⁴ Advanced Energy Storage Products Quality Supervision and Inspection Center, 8 Chunxin East Road, Wuxi, 214101, P. R. China

*E-mail: wangyaping@ujs.edu.cn

Received: 3 November 2020 / *Accepted:* 22 December 2020 / *Published:* 31 January 2021

To enable a battery to operate in a suitable temperature range, a three-dimensional electrochemical-thermal fully coupled model of a cylindrical lithium-ion battery (LIB) including a spiral wound structure is constructed. The precise temperature distribution and transient heat generation rate inside the battery are obtained by considering charge conservation, mass transfer, energy conservation and electrode dynamics processes. Based on the constructed model, a semi-enclosed S-shaped surrounding structure is proposed to dissipate the heat of the battery module. The effects of cooling channel height, width and inlet velocity on the heat dissipation performance are studied. The height of the cooling channel is close to the height of the active material, which can affect both the cooling performance and portability of the liquid cooling device. Meanwhile, when the width of the liquid cooling channel is 3 mm, it not only has the best cooling effect but also improves the space utilization, and when the inlet velocity is more than 0.15 m/s, the maximum temperature and temperature difference of the module during the entire discharge process can be kept under 303 K and 5 K. In addition, by considering the thermal conductivity differences between the axial and radial directions of the active material, a decentralized optimization design of multiple cooling channels in the vertical direction is proposed. The results show that a structure with three channels in the vertical direction and a height of the middle channel twice that of the upper and lower ones is more favourable for heat transmission from the inside to the outside because it disperses the heat dissipation surface area to improve the temperature consistency of the module and effectively improves the heat dissipation performance of the liquid cooling structure.

Keywords: Lithium-ion battery; Electrochemical-thermal coupled; Liquid cooling; Structural optimization

1. INTRODUCTION

Global energy shortages and environmental pollution are driving the development of new energy vehicle technology [1]. At present, a variety of batteries, including lead-acid batteries, Ni-MH batteries and lithium-ion batteries (LIBs), have been proposed for use in electric vehicles and hybrid vehicles. In recent years, an increasing number of automotive manufacturers have benefited from ternary LIBs because of their low self-discharge rate, long cycle life, and high specific energy density and voltage (operating voltage 3.6-3.7 V) [2-5]. However, LIBs are very sensitive to ambient temperature. When the ambient temperature is too low, the movement rate of Li^+ will decrease, and the internal resistance of LIBs will increase rapidly, which decreases the charge and discharge capacity significantly. When the ambient temperature is too high, a series of chemical reactions will accumulate and strengthen each other, generating much heat, which can easily lead to thermal runaway, fires, explosions and other safety accidents [6-8]. In addition, due to the volume limitations in new energy vehicles, battery modules are usually sealed in narrow battery boxes. A local temperature that is too high or too low will result in a reduced cycle life [9]. Research has shown that the optimal operating temperature for LIBs is 20-40 °C, and the temperature difference (ΔT) of the battery pack should be controlled below 5 °C [10]. Jia et al. [11] proposed a one-dimensional electrochemical-thermal coupled model to simulate several galvanostatic discharge processes under different physical conditions. It was found that as the discharge rate increased, the nonuniformity of the heat generation and electrochemical reaction rate in the battery increased. Therefore, to keep the battery within the optimal operating temperatures at all times, a reliable and efficient thermal management system is essential.

At present, battery thermal management can be characterized air cooling, liquid cooling, phase change material cooling, and heat pipe cooling systems according to the heat transfer medium [12]. Air cooling removes the heat in the battery box through natural air convection or forced convection by a fan. Air cooling systems have simple structures and are low cost, but the maximum temperature of a battery pack cannot be controlled at 50 °C at a large discharging rate [13]. Atta Sojoudi et al. [14] immersed cylindrical LIBs in a thin cylindrical tank, and air cooling was used to remove heat. CFD was used to simulate 36 different inlet and outlet airflow positions and nine different battery arrangements. The results showed that the new method effectively reduced the maximum temperature of the battery. When phase change cooling is used, the phase change material can absorb a large amount of latent heat during the melting process, effectively reducing the temperature of the battery pack, but the structural strength of the material is weak. In addition, the thermal conductivity and the surface heat transfer coefficient are relatively low [15,16]. The structural design of heat pipe cooling is complex, and it is still consigned to the research and development stage.

Compared with air cooling, liquid cooling has a higher thermal conductivity, which can effectively improve heat dissipation efficiency [17]. Liquid cooling has been extensively studied by scholars from various countries. Yang et al. [18] proposed a single-factor analysis and orthogonal test to investigate the influence of coolant inlet speed, the number of channels and contact angle on cooling performance. The contact angle had the most significant effect and should be fixed at approximately 70°. The appropriate values of inlet speed and number of channels have varied within the range of 0.2-0.5 $\text{m}\cdot\text{s}^{-1}$ and 1-2, respectively. Wang et al. [19] proposed a thermally conductive structure (TCS) with three

curved contact surfaces to cool cylindrical batteries. The study found that during a 5 C discharge, T_{\max} could be maintained within 313 K, and the inner diameter was the most important factor affecting the weight of the device. Jiang et al. [20] proposed two solutions: (a) shortening the flow path by using multiple serpentine channels and (b) increasing the contact areas along the flow path. Numerical simulation results showed that these two methods could effectively reduce the thermal nonuniformity of the battery module. [21] Rao et al. designed a new liquid cooling structure for a cylindrical LIB module with a variable contact surface. The effects of aluminium block length and cooling water flow rate on the thermal performance were studied. The results showed that a variable contact surface system was better than a constant contact surface system. Zhou et al. [22] proposed a liquid cooling method based on a half-helical structure. The effects of inlet mass flow, fluid flow direction, pitch and number of helical ducts and spiral tube diameter on the thermal performance were numerically analysed. When the inlet mass flow rate was 3×10^{-4} kg/s, the diameter of the semispiral duct ranged between 2.0 and 3.8 mm, the temperature difference was kept within 4.3 °C, and the maximum temperature was close to 30.9 °C.

Much research has been done on the liquid cooling system of LIB packs, and much progress has been made. Most studies used a lumped model that generally adopted constant entropy heat coefficients and did not fully consider the complex electrochemical reaction of the battery during the charging and discharging process when calculating the heat generation rate. Only a few studies have adopted the research strategy of combining the battery electrochemical and thermal models rather than be limited to a one-dimensional model. To obtain the accurate temperature distribution of a single cell, a three-dimensional electrochemical-thermal fully coupled finite model was established in this work [23-25]. Compared with traditional one-dimensional and two-dimensional electrochemical models [26-27], the three-dimensional electrochemical model fully considers the edge effect on the battery length and height, showing more details inside the battery. In addition, the finite element model does not need to consider the battery active material area as a whole during calculation and does not need to use the average specific heat capacity, density and thermal conductivity. The three-dimensional electrochemical model established in this paper can fully consider the complex chemical reactions inside the battery to obtain a more accurate temperature distribution.

By disassembling a SONY 18650 single cell and consulting the battery manufacturer, a detailed geometric model of the battery is constructed. The three-dimensional fully coupled model used in this study includes a spiral wound structure of positive and negative electrodes, positive and negative current collectors, and a separator. Combining charge conservation, mass transfer, energy conservation, and electrode dynamics, an accurate temperature distribution inside the battery is obtained. In addition, this paper proposes a semi-enclosed S-shaped surrounding structure, which greatly increases the contact area between the cooling channel and the battery. In addition, by considering the thermal conductivity differences between axial and radial active materials, a decentralized optimization design of multiple cooling channels in the vertical direction is proposed. The use of multiple cooling channels in the vertical direction disperses the heat dissipation area of the battery surface, which effectively improves the heat dissipation efficiency of the whole module. The flow chart of the content and technical procedure is shown in Figure 1.

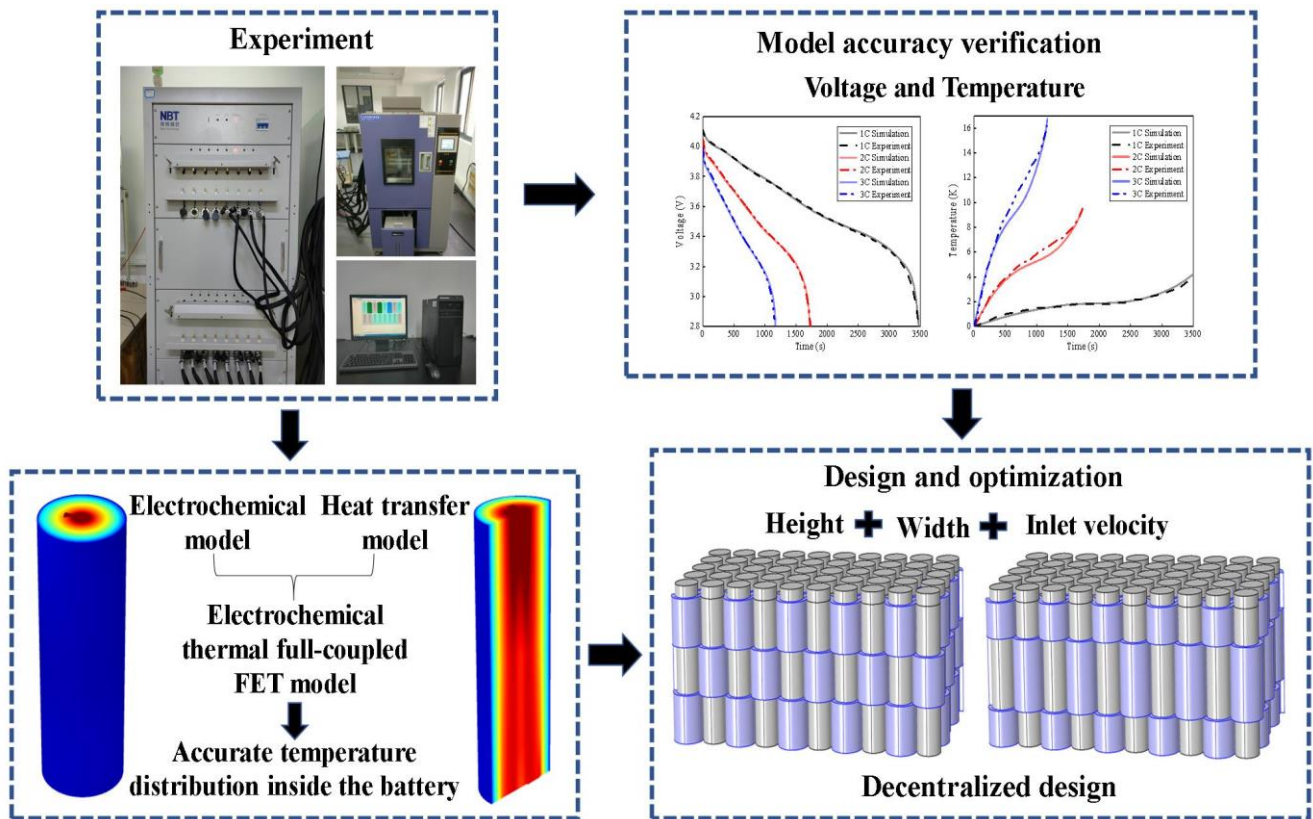


Figure 1. Flowchart of the content and technical route procedure.

Nomenclature			
ρ	density (kg/m^3)	h	Heat transfer coefficient ($\text{W}/(\text{m}^2/\text{K})$)
c_p	specific heat capacity ($\text{J kg}^{-1} \text{K}^{-1}$)	t_+^0	Lithium ion transfer number
k	thermal conductivity ($\text{W}\cdot\text{m}^{-1}\cdot\text{K}^{-1}$)	k^{eff}	Effective ion conductivity (S/m)
u	velocity vector	α	Transfer coefficient
P	static pressure	φ	Electric potential (V)
μ	dynamic viscosity	j_{Li}	Local current density (A/m^2)
T	temperature	ν	Thermodynamic factor
T_{max}	maximum temperature (K)	σ_2	Liquid phase conductivity (S/m)
ΔT_{max}	maximum temperature difference (K)	D_i	Ion diffusion coefficient (m^2/s)
ε_1	Volume fraction of solid	r	Radius of particle (μm)

ϵ_2	Volume fraction of electrolyte	l	Thickness of each part (μm)
cc	Current collector	c	Concentration (mol/m^3)
eff	Effective	re	Reversible
act	Active polarization	sep	Separator

2. MODEL AND VERIFICATION

2.1 Design of the liquid cooling structure

The battery module in this study consists of 50 cylindrical batteries, and the liquid cooling system of the battery module is shown in Figure 2. The 50 cells are numbered as shown in Figure 2c, and the cell numbers are increased successively along the direction of coolant flow from the No. 1 cell at the inlet. The liquid cooling channel is a semi-enclosed S-shaped surrounding structure with an arc angle of 180° . The inner wall of the liquid cooling channel is kept in close contact with the batteries. The width of the liquid cooling channel is (x) mm. The height of the liquid cooling channel is (y) mm. The liquid cooling channel is made of aluminium, and the thickness of the inner and outer sidewalls is 0.2 mm. Water is used as the cooling liquid. When the inlet velocity of the water is the maximum value of 0.2 m/s, the Reynolds number calculated by fluid mechanics is less than 2000, and the flow of water in the cooling channel is considered to be laminar. It is assumed that the energy conservation principle is followed in the liquid cooling process. The aluminium liquid cooling channel transfers the heat generated by the batteries to the cooling water, and the laminar flow of water in the cooling channel removes the heat. $ht.dEi0Int$, $ht.ntefluxInt$ and $ht.QInt$ represents the heat accumulated in the module, the heat taken away by the water, and the total heat produced in the module. According to the energy conservation principle, each moment of the module meets the equation $ht.dEi0Int + ht.ntefluxInt = ht.QInt$. The heat data at all times during the discharge process are shown in Table 1. The numerical simulation uses the multiphysics simulation software COMSOL5.5.

Table 1 Heat at all times during discharge.

Time (s)	$ht.QInt$ (W)	$ht.dEi0Int$ (W)	$ht.ntefluxInt$ (W)
0	40.706	40.706	0
200	78.634	-1.014	79.648
400	60.150	-5.033	65.183
600	55.327	-1.237	56.564
800	55.470	0.062	55.409
1000	57.990	1.821	56.169
1165.3	118.52	31.978	86.540

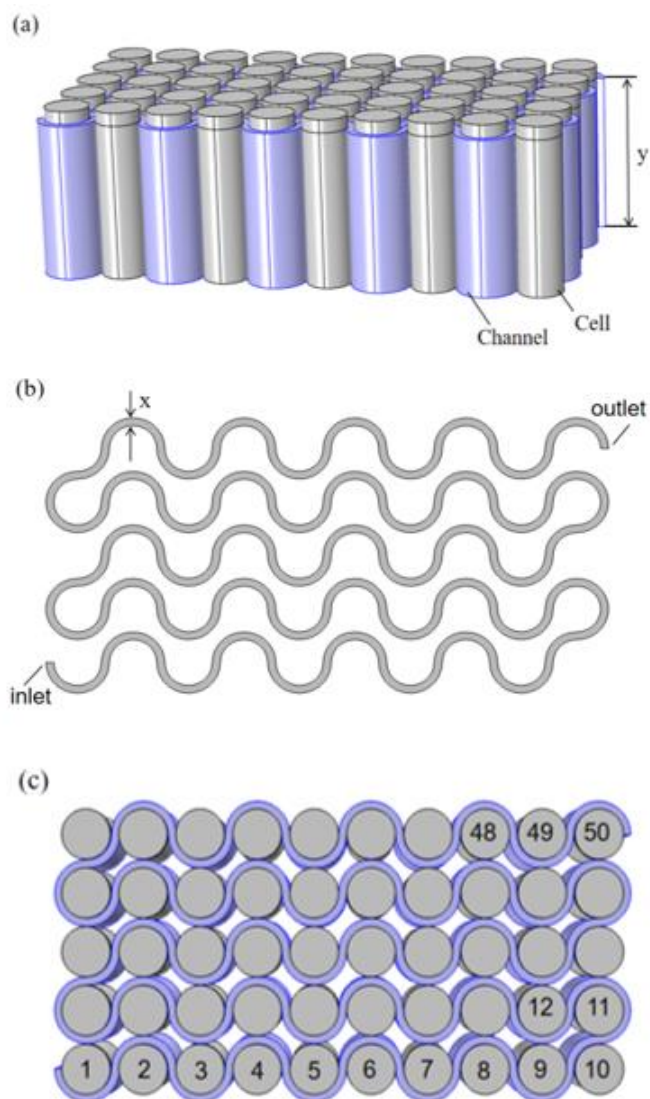


Figure 2. Schematic diagram of (a) the battery module, (b) the cooling channel, and (c) top view of the battery module.

2.2 Boundary conditions and grid independence test

The boundary conditions of the inlet and outlet are set as the velocity inlet and pressure outlet, respectively. The relative pressure at the outlet is set to zero, and channel wall conditions are set to no slip. All the surfaces are taken as adiabatic boundary conditions. The battery module and initial coolant temperature are set at 25 °C. To ensure the accuracy of the simulation results, grid independence testing is indispensable. In this paper, the heat transfer rate is used to test the independence of the grid number. Figure 3 shows the calculation results of different grid numbers. When the grid number is increased from 222537 to 650315, the value of the heat transfer rate is only reduced by 0.23%. Therefore, the number of grids selected in this study is 222537.

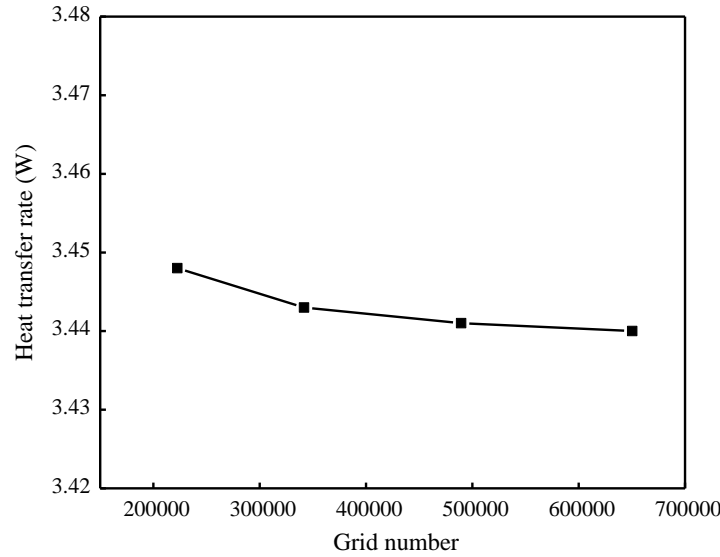


Figure 3. Independence test of grid number

2.3 Electrochemical thermal model for a single cell

Table 2 The governing equations of the electrochemical-thermal coupled model and boundary conditions

Governing Equations	Boundary Conditions
Mass Conservation:	
Solid Phase: $\frac{\partial c_1}{\partial t} = D_1(\frac{\partial^2 c_1}{\partial r^2} + \frac{2}{r} \frac{\partial c_1}{\partial r})$	$\frac{\partial c_1}{\partial r} \Big _{r=0} = 0; -D_1 \frac{\partial c_1}{\partial r} \Big _{r=R} = j_{Li}$
Liquid Phase: $\varepsilon_2 \frac{\partial c_2}{\partial t} = \nabla(D_2^{eff} \nabla c_2) + \frac{1-t_+^0}{F} j_{Li}$	$\frac{\partial c_2}{\partial x} \Big _{x=l_{pos,cc}} = \frac{\partial c_2}{\partial x} \Big _{x=l_{tot}-l_{neg,cc}} = 0$
Charge Conservation:	
Solid Phase: $\nabla(\sigma^{eff} \nabla \phi_1) = j_{Li}$	$\varphi_{cc} \Big _{x=l_{tot}} = 0; -\sigma_{cc} \frac{\partial \varphi_{cc}}{\partial x} \Big _{x=0} = -I_{tot} / n$
Liquid Phase: $\nabla\{k^{eff} [-\nabla \phi_2 + \frac{2RT}{F}(1 + \frac{\partial \ln f}{\partial \ln c_2})(1-t_+^0) \frac{\nabla c_2}{c_2}]\} = j_{Li}$	$\frac{\partial \varphi_1}{\partial x} \Big _{x=l_{pos,cc} + l_{pos}} = \frac{\partial \varphi_1}{\partial x} \Big _{x=l_{pos,cc} + l_{pos} + l_{sep}} = 0$
Electrochemical Kinetics:	Phase: $\frac{\partial \varphi_2}{\partial x} \Big _{x=l_{pos,cc}} = \frac{\partial \varphi_2}{\partial x} \Big _{x=l_{tot} - l_{neg,cc}} = 0$
$j_{Li} = \alpha_v i_0 [\exp(\frac{\alpha_a F}{RT} \eta) - \exp(-\frac{\alpha_c F}{RT} \eta)]$	
$i_0 = FK(c_2)^{\alpha_a} (c_{1,max} - c_{1,surf})^{\alpha_a} (c_{1,surf})^{\alpha_c}$	
Thermal Model: $\rho C_p \frac{\partial T}{\partial t} = \nabla(\lambda \nabla T) + Q$	
$Q = Q_{re} + Q_{ohm} + Q_{act}$ $Q_{re} = j_{Li} T \frac{\partial U}{\partial T}$	
$Q_{act} = j_{Li} (\phi_1 - \phi_2 - U_{eq})$	
$Q_{ohm} = \sigma^{eff} (\nabla \phi_1)^2 + k^{eff} (\nabla \phi_2)^2 + \frac{2RTk^{eff}}{F} (t_+^0 - 1) (1 + \frac{\partial \ln f}{\partial \ln c_2}) \nabla(\ln c_2) \nabla \phi_2$	

Based on energy conservation, mass conservation, charge conservation and electrochemical dynamics, a 3D electrochemical-thermal fully coupled model for NCM/graphite batteries is established. During the model building process, the following assumptions are made:

1. During the charging and discharging process, no gas is generated, that is, no gas phase is generated, and only the solid phase and liquid phase are considered;
2. No side reactions occur during the whole process;
3. The particle sizes of the active material and the electrode slurry are uniform;
4. The volume expansion during the reaction and its internal stress changes are not considered.

According to the above assumptions, as well as the diffusion and migration rules of Li^+ in the solid and liquid phases and Ohm's law, the corresponding governing equations are established [28-29]. The governing equations of the electrochemical-thermal coupled model and boundary conditions are shown in Table 2. Figure 4 shows the temperature rise of the fully coupled model established at a 2 C discharge rate.

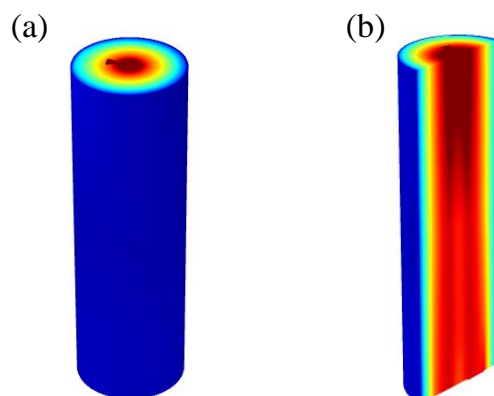


Figure 4. (a) Temperature rise of the overall view and (b) sectional view at 2 C discharge.

2.4 Physical model of battery module

The governing equation of energy conservation of the battery pack is as follows:

$$\frac{\partial}{\partial t}(\rho_b c_{p,b} T_b) = \nabla \cdot (k_b \nabla T_b) + Q \quad (1)$$

where ρ_b is the density of the battery; T_b is the temperature of the battery; $c_{p,b}$ is the specific heat capacity of the battery; and k_b is the thermal conductivity of the battery. The cooling liquid is water, and the flow of water is considered to be laminar by the Reynolds number calculation. The mass conservation, momentum conservation and energy conservation equations for water are:

$$\frac{\partial \rho_c}{\partial t} + \nabla \cdot (\rho_c u) = 0 \quad (2)$$

$$\frac{\partial}{\partial t}(\rho_c u) + \nabla \cdot (\rho_c uu) = -\nabla P + \nabla \cdot (\mu \nabla u) \quad (3)$$

$$\frac{\partial}{\partial t}(\rho_c c_{p,c} T_c) + \nabla \cdot (\rho_c c_{p,c} u T_c) = \nabla \cdot (k_c \nabla T_c) \quad (4)$$

where u , P and μ denote the coolant velocity vector, static pressure and dynamic viscosity, respectively. ρ_c , $c_{p,c}$, k_c and T_c are the density, specific heat capacity, thermal conductivity and temperature of the coolant, respectively.

2.5 Thermal behaviour of the cell

In this study, commercial SONY 18650 LIBs are used. The thermal physical parameters and geometric parameters of the battery are shown in Table 3. To verify the accuracy of the single-cell model, an NBT battery tester system (NBT30V100AC4-T) is used to charge and discharge the battery in a constant temperature and humidity environment. The experimental setup is shown in Figure 5. Three cylindrical batteries of the same batch are selected for testing to ensure the reliability of the data. Three T-type thermocouples (accuracy ± 0.1 K) are fixed to the middle of the outer surfaces of three cylindrical batteries with insulating tape. The experimental data are recorded by an Agilent 34970A Data Logger. The average value of the data obtained from the three thermocouples is used as the temperature on the outer surface of the battery.

Table 3 Thermo-physical properties of battery materials/components and geometric parameters of the battery [29,30].

Parameters	Thickness (μm)	Height (mm)	Density (kg/m^3)	Thermal conductivity ($\text{W} \cdot \text{m}^{-1} \cdot \text{K}^{-1}$)	Specific heat capacity ($\text{J kg}^{-1} \text{K}^{-1}$)
Pos	50	58	4700	1.58	1269.21
Neg	54	69	2270	1	881
Sep	18	60.5	1200	1	700
Anode foil	10	60	2700	238	900
Cathode foil	15	59	8960	400	385
Electrolyte	N/A	N/A	1290	0.45	133.9

The experimental process is as follows: First, the battery is fully charged with constant current and constant voltage. After standing for 1 hour, 1 C, 2 C, and 3 C constant currents were used to discharge to a cut-off voltage of 2.8 V at an ambient temperature of 298.15 K. Figure 6a shows that the discharge curve of the battery matches the simulation well. Figure 6b shows that the surface temperature of the battery during discharge is in good agreement with the data calculated by the model. The comparison results show that the electrochemical-thermal coupling model is accurate and reasonable.



Figure 5. Battery Tester System (NBT30V100AC4-T): (a) NBT test equipment (b) Incubator (c) Computer.

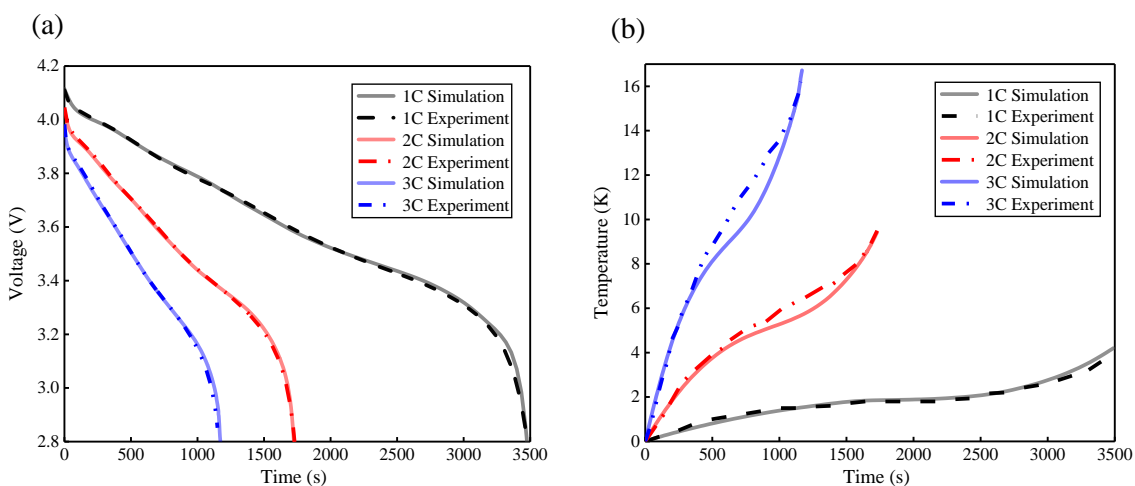


Figure 6. (a) Voltage and (b) temperature comparison of the experimental data and the simulation results.

3. RESULTS AND DISCUSSION

The structure of the liquid cooling system and the inlet velocity are closely related to the heat dissipation of the battery module. Jarret [30] simulated the heat dissipation of a battery module under various flow channel shapes and found that the shape of the flow channel, the width of the flow channel and the inlet velocity influenced the heat dissipation effect of the module. Therefore, the influence of the

channel height, channel width and inlet velocity on the heat dissipation of the module is analysed. The maximum temperature T_{\max} of the module and the maximum temperature difference ΔT_{\max} between the battery cells are mainly used as the evaluation indexes for the cooling performance.

3.1 Effects of channel height

This section mainly studies the effect of different channel heights on T_{\max} and ΔT_{\max} . The width of the channel is fixed at 2 mm, the inlet velocity is set at 0.025 m/s, and the module discharges at a 3 C constant current. The heights of the cooling channel are set as 50, 55, 60, and 65 mm. The T_{\max} and ΔT_{\max} during discharge are shown in Figure 7. It can be seen that the values of T_{\max} and ΔT_{\max} have a similar change trend throughout the discharge process, which can be roughly divided into three stages. At the initial 0-400 s of discharge, the T_{\max} of the battery module rises sharply, and the T_{\max} rise rate with different channel heights is basically the same. During 400 s-1000 s in the middle of discharge, the ascent rate of T_{\max} slows down significantly. The higher the height of the cooling channel is, the more obvious the T_{\max} slows down; it gradually reaches a larger value at approximately 500 s and then begins to slowly decrease. At the end of the discharge from 1000 s to 1200 s, as the heat generation rate increases, T_{\max} rises rapidly again and reaches the maximum value at the end of the discharge. During the entire discharge process, the minimum temperature of the module is always near the inlet, which basically remains unchanged. Therefore, the change in T_{\max} determines the change trend of ΔT_{\max} . It can be seen in the figure that the increase in the channel height increases the contact area between the cooling channel and the battery, which effectively improves the heat dissipation efficiency. The values of T_{\max} and ΔT_{\max} gradually decrease with increasing channel height, and the rate of decrease gradually slows down. When the channel height increases from 60 mm to 65 mm, at the end of the discharge, T_{\max} and ΔT_{\max} only decrease by 0.34 K and 0.25 K, respectively.

By disassembling the battery, it is found that the height of the active material inside the battery composed of the positive electrode, positive current collector, separator, negative electrode and negative current collector is approximately 60 mm, and the height of the top battery cover is 5 mm. During the charging and discharging process, the battery mainly generates heat through the electrochemical reaction between active materials. When the height of the channel reaches 60 mm, a further increase in the height has little effect on the heat dissipation. Considering the cooling performance and the portability of the liquid cooling device, the channel height is chosen to be 60 mm. When the channel height is 60 mm, the T_{\max} and ΔT_{\max} of the module at the end of the discharge are 306.23 K and 8.49 K, respectively. However, the entire module still cannot operate in the optimal temperature range. Therefore, the influence of the channel width on the cooling performance will be discussed below.

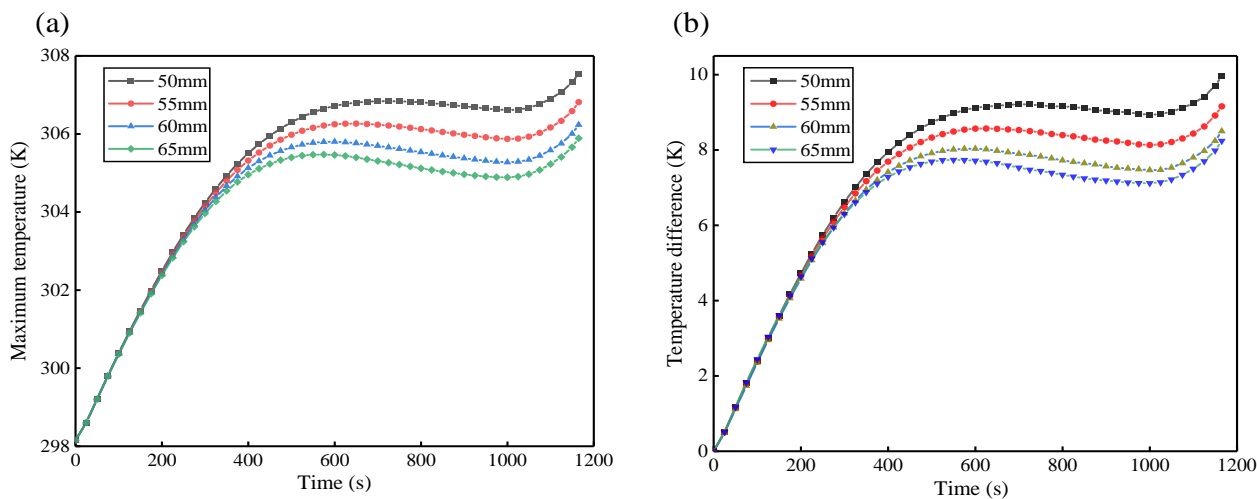


Figure 7. The (a) maximum temperature T_{\max} and (b) maximum temperature difference ΔT_{\max} of the module with various channel heights.

3.2 Effects of channel width

The height of the liquid cooling channel is fixed at 60 mm, the inlet velocity is set at 0.025 m/s, and the module discharges at a 3 C constant current. This section mainly studies the influence of different channel widths on T_{\max} and ΔT_{\max} . The widths of the cooling channels are set as 1, 2, 3, and 4 mm. T_{\max} and ΔT_{\max} are shown in Figure 8.

The effect of the channel width on the cooling performance of the module is similar to the channel height. At the beginning of discharge, T_{\max} increases rapidly. Except for the width of 1 mm, using other width cooling channels, T_{\max} will reach a high point in the middle of the discharge and then enter a relatively stable platform period. It will increase rapidly again near the end of the discharge and reach the maximum value at the end of the discharge. When the channel width is 1 mm, T_{\max} always maintains a relatively high growth rate. There is no obviously stable stage during the entire discharge process, indicating that when the width is 1 mm, the module cannot be effectively cooled from beginning to end. At the end of the discharge, the T_{\max} and ΔT_{\max} of the module reach 311.05 K and 12.77 K, respectively. Figure 8c shows the temperature contour of the module at the end of the discharge process with a 1 mm channel width. Figure 8d and Figure 8e show the temperature contours of the 1 mm and 3 mm channels at the end of the discharge (XY plane, $Z = 30$ mm). As seen in Figure 8c, when the channel width is 1 mm, the first two rows of batteries (1-20) near the entrance have a lower temperature and better temperature consistency. However, the battery arrangement is crowded, and the channel width is narrow. The coolant is easily heated by the heat generated by the battery and cannot effectively remove the heat generated by the module. As the temperature of the cooling fluid gradually increases in the direction of the flow path, the cooling effect on the battery becomes significantly worse. The temperature of the last row of batteries 41-50 near the outlet increases significantly, and the unevenness in temperature between cells increases greatly. When the width of the channel is 3 mm, the heat generated by the battery is not enough to quickly heat the coolant. The temperature rise of the cooling liquid along the flow path is significantly slower. When the channel width increases from 1 mm to 2 mm, T_{\max} and ΔT_{\max} decrease

significantly from 300 s. At the end of the discharge, the channel width is reduced by 4.82 K and 4.8 K when compared with the channel width of 1 mm. As the width increases, the rate of decrease gradually slows down. Changing the channel width from 3 mm to 4 mm, T_{max} and ΔT_{max} only decrease by 0.78 K and 0.76 K at the end of the discharge, respectively, while the occupied space increases by 11%. Therefore, the channel width is set as 3 mm. When the channel width is 3 mm, the T_{max} and ΔT_{max} of the module at the end of the discharge are 305.03 K and 6.75 K, respectively. The whole module is still unable to operate in the optimal temperature range, so the effect of coolant inlet velocity on cooling performance will be discussed below.

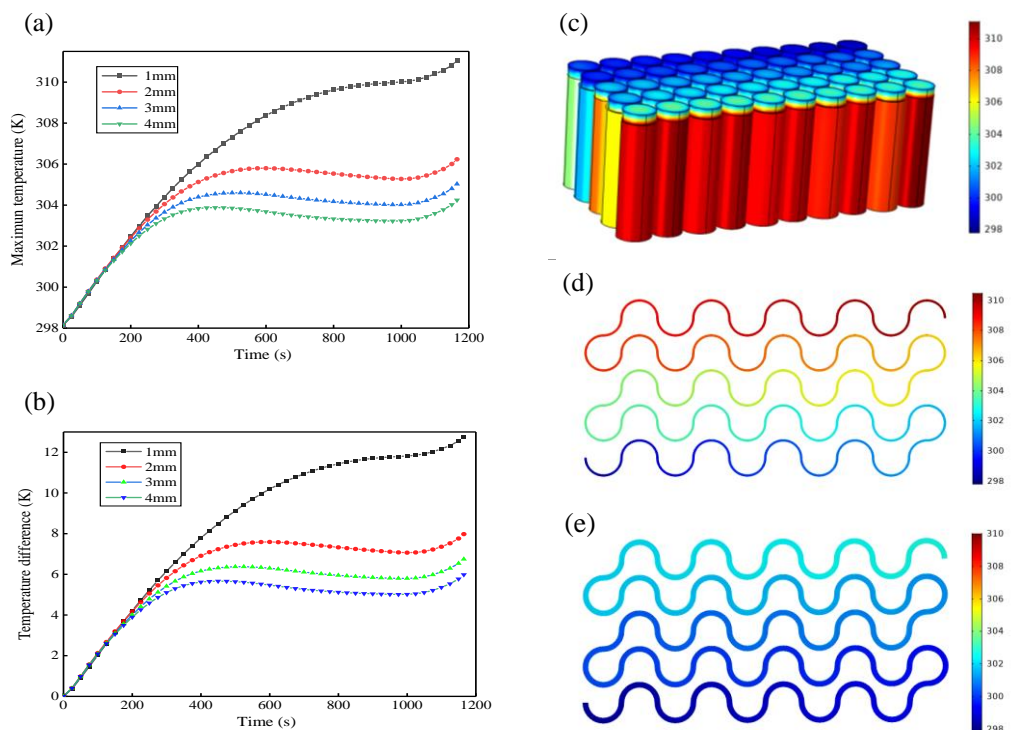


Figure 8. The (a) T_{max} and (b) ΔT_{max} of the module with various channel widths. (c) The temperature contour of the module at the end of the discharge process with a 1 mm channel width and the temperature contours (XY plane, Z=30 mm) of the channel at the end of the discharge process with a (d) 1 mm and (e) 3 mm channel width.

3.3 Effects of inlet velocity

The width of the liquid cooling channel is fixed at 3 mm, and the module discharges at a 3 C constant current. The inlet velocity is critical to the cooling performance of the battery module [31-33]. This section mainly studies the effect of different inlet velocities on T_{max} and ΔT_{max} , using 0.025 m/s, 0.05 m/s, 0.075 m/s, 0.1 m/s, 0.15 m/s and 0.2 m/s as the coolant inlet velocities. Figure 9a and Figure 9b show the T_{max} and ΔT_{max} of the module with different inlet velocities. At the initial stage of discharge, regardless of the inlet flow rate, T_{max} and ΔT_{max} rapidly increase in an approximate straight line. This is mainly because the temperature difference between the battery and the cooling water is small, and it is difficult for the cooling water to remove the rapidly increased heat generated by the battery module. In

the middle of the discharge, T_{\max} and ΔT_{\max} reach a higher value and begin to decline slowly, indicating that the heat taken away by the water exceeds the heat generated by the module. At the end of the discharge, T_{\max} and ΔT_{\max} again increase rapidly and reach the maximum value of the entire discharge process. This is mainly due to the intensified electrochemical reaction inside the battery near the end of discharge. Figure 9 shows that the larger the inlet velocity is, the slower the rise rate of T_{\max} and ΔT_{\max} during the early stage of discharge. In the middle and later periods, the same trend is maintained. When the inlet velocity increases from 0.025 m/s to 0.05 m/s, T_{\max} and ΔT_{\max} decrease by 1.71 K and 2.14 K at the end of discharge, respectively. As the inlet flow rate increases, the decrease rate gradually slows. When the inlet velocity increases from 0.15 m/s to 0.2 m/s, T_{\max} and ΔT_{\max} only decrease by 0.16 K and 0.14 K at the end of discharge.

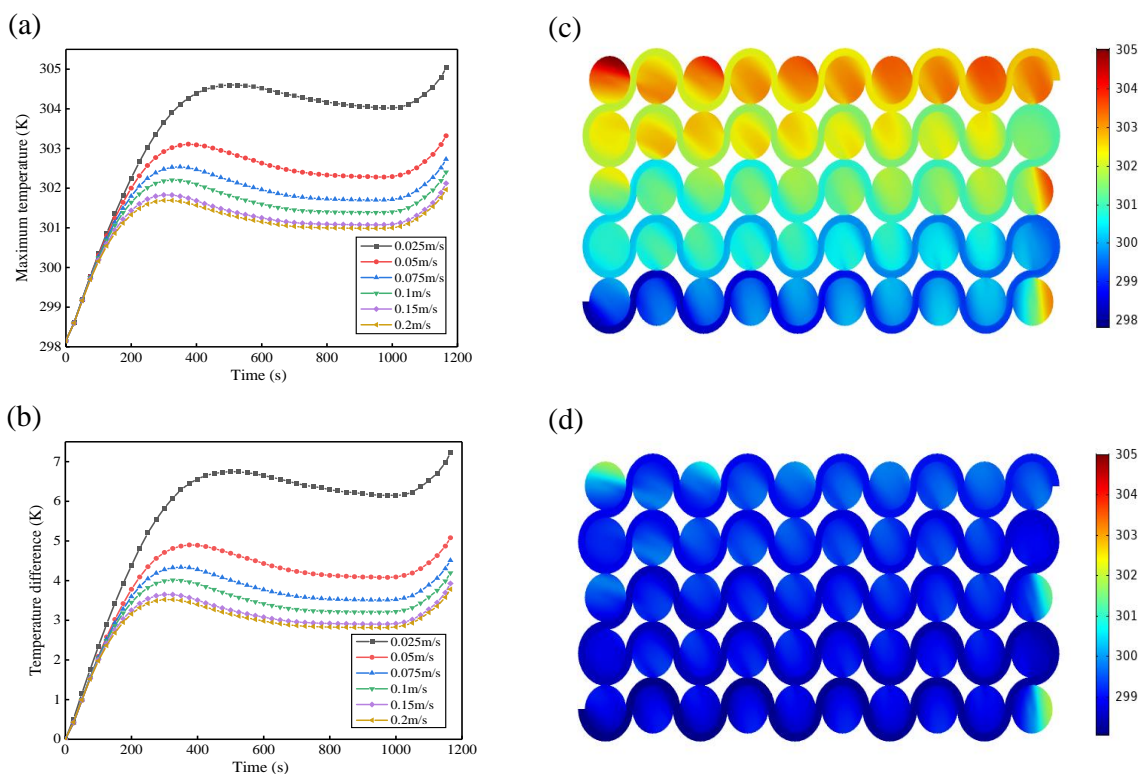


Figure 9. The (a) maximum temperature (T_{\max}) and (b) maximum temperature difference (ΔT_{\max}) of the module with various inlet velocities. The temperature contours (XY plane, $Z=30$ mm) of the module at the end of the discharge process with (c) 0.025 m/s and (d) 0.2 m/s inlet velocities.

Figure 9c and Figure 9d show the temperature contours (XY plane, $Z=30$ mm) at the end of the discharge process with inlet velocities of 0.025 m/s and 0.2 m/s. Figure 9c shows that the inlet velocity is 0.025 m/s, and there is a clear temperature gradient along the flow path from the inlet to the outlet. When the inlet velocity is 0.2 m/s (Figure 9d), the entire module maintains good temperature consistency. It can be concluded that the larger the inlet velocity of the coolant is, the longer the path that flows through at the same time; more battery heat is taken away, which leads to a better cooling performance. However, an excessive increase in the inlet velocity will cause a sharp increase in the pressure difference between the inlet and outlet, resulting in a significant increase in pump power. Therefore, excessively

increasing the inlet velocity is not a sensible solution. Next, the design structure will be optimized to improve the temperature consistency of the module.

3.4 Improvement and optimization

From the research above, it is found that the maximum temperature of the entire module always appears near the No. 40 battery, mainly because the No. 40 battery is located on the outermost side of the entire module and has only 1/4 of the outer surface contact area with the liquid cooling channel. Therefore, to solve the problem of a large temperature rise caused by the small contact area between the outermost batteries and the liquid cooling channel, an improved structure in which the upper and lower liquid cooling channels wrap the batteries complementarily is proposed.

As shown in Figure 10a, the height of the two liquid cooling channels is equal to 30 mm, and the width of the cooling channel is fixed at 3 mm. The entrances of the two channels adopt two layout schemes: (c) on the left and right sides and (d) on the same side.

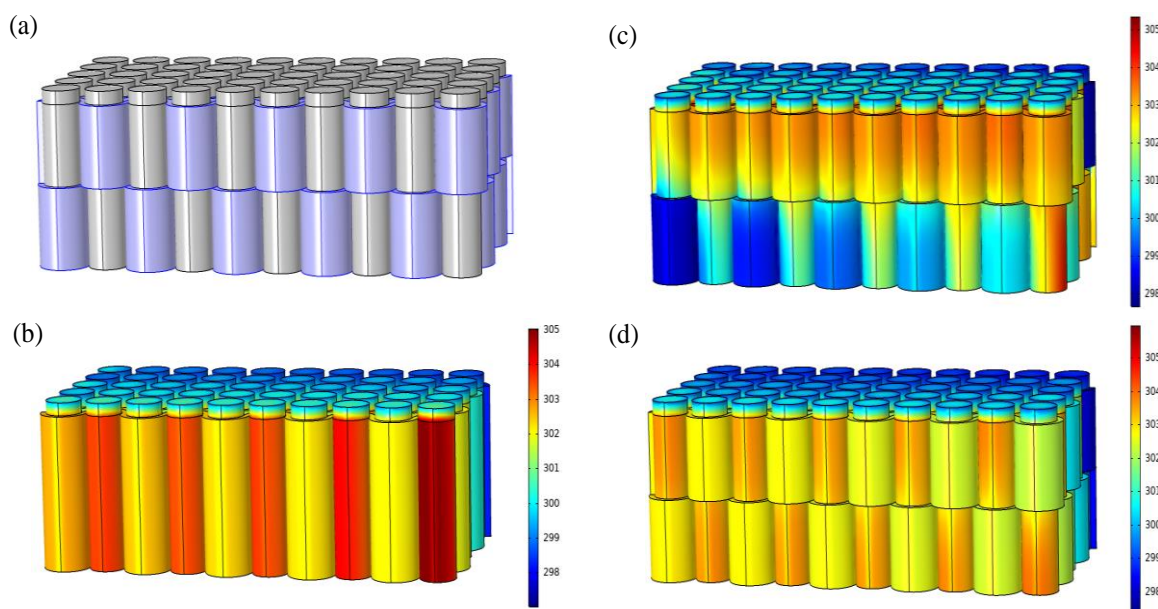


Figure 10. (a) The optimized schematic diagram of the battery module, (b) the temperature contours of only one channel, (c) the temperature contours of entrances of the two channels on the left and right sides and (d) the temperature contours of entrances of the two channels on the same side

The inlet velocity is fixed as 0.025 m/s. Figure 10 shows that the improved structure significantly reduces the temperature of the outermost battery, effectively reduces the maximum temperature of the entire module and improves the overall temperature consistency. Comparing Figure 10c and Figure 10d, it is found that when the inlets of the upper and lower cooling channels are located on the left and right sides, the last row of batteries (Nos. 41-50) shows a significant temperature difference between the upper and lower parts. The lower half of the battery is closer to the inlet of the lower cooling channel, so the

temperature is lower. The upper half of the battery is closer to the outlet of the upper cooling channel, so the temperature is higher. Thus, there is a large temperature difference between the upper and lower parts. This uneven temperature distribution will cause the performance and cycle life of the single cell to be greatly reduced, so it is decided to use the design with the entrance on the same side, which has a better cooling effect. Compared with the structure with only one liquid cooling channel, the T_{\max} and ΔT_{\max} of two channels with inlets on the same side design drop by 1.07 K and 0.96 K.

Combined with the above research, the cooling channel is further refined into three cooling channels: upper, middle and lower. Figure 11c shows that the upper, middle and lower three channels have the same height of 20 mm. The height of the middle channel is twice that of the upper and lower channels, and the upper and lower channels are both 15 mm in Figure 11d. The coolant inlets are located on the same side of the module. The thickness of the cooling channel is 3 mm, and the total height of the channel is 60 mm. The maximum temperature and temperature difference at the end of the 3 C discharge of the module are shown in Table 4. Design 1 has only one cooling channel, and the height is 60 mm. Design 2 has two channels, upper and lower, and both heights are 30 mm. Design 3 has three cooling channels in the upper, middle and lower regions, and all have the same height of 20 mm. Design 4 uses a structure where the middle channel is twice the height of the upper and lower channels. As seen in Table 4, compared with Design 1, the maximum temperature of the module in the latter three improved designs is significantly lower, and the overall temperature consistency is better. This is because for a single cell in the module, such as the No. 2 battery, the liquid cooling channel of Design 1 is only in contact with the rear half surface of the battery. The heat of the untouched front half surface cannot be quickly transferred to the rear half, so the front half surface cannot be effectively cooled. Although Design 2 does not increase the contact area between the No. 2 battery and the cooling channel compared with Design 1, the two liquid cooling channels divide the outer surface of the battery into upper and lower parts. This helps disperse the heat dissipation area of the No. 2 battery so that the heat of the battery will not accumulate in the entire front half. Due to the differences in axial and radial thermal conductivity of the internal active material, this decentralized design is more conducive to the conduction of heat from the inside to the outside. In addition, the design of the upper and lower complementary wrapping can effectively solve the shortcomings of the small contact area between the outermost batteries and the cooling channel. Designs 3 and 4 also have a better cooling effect than Design 2. Compared with Design 2, the T_{\max} and ΔT_{\max} of Design 4 are reduced by 0.35 K and 0.48 K. This is mainly because Designs 3 and 4 further disperse the heat dissipation area of the battery surface compared to Design 2. The difference between the axial and radial thermal conductivity makes the heat of the battery easier to remove by the closer cooling channel, which further reduces the module overall temperature. In Design 3, half of the batteries have only 1/3 of the front half of the surface in contact with the cooling channel, while the other half have only 1/3 of the rear half of the surface in contact with the cooling channel. The uneven heat dissipation area of the front and rear surfaces makes the heat dissipation performance of Design 3 slightly worse than that of Design 4. Therefore, using multiple cooling channels in the vertical direction can disperse the heat dissipation area of the battery surface without directly increasing the contact area. This improved design effectively improves the heat dissipation performance of the liquid cooling system and significantly reduces the maximum temperature of the battery at the edge of the module. Compared with the variable contact area liquid cooling structure proposed by Rao [21] and

increasing the number of channels design proposed by Huo [34], the decentralized liquid cooling design used in this paper significantly reduces the maximum temperature of the module. In addition, the decentralized optimization design greatly improves the overall temperature consistency of the module and reduces the temperature difference between single batteries compared with research by Zhao [35] and Zhang [36]. Last but not least, compared with results of Tong [37] and Zhao [38], the improved model uses a smaller coolant inlet velocity, which significantly reduces pump power loss.

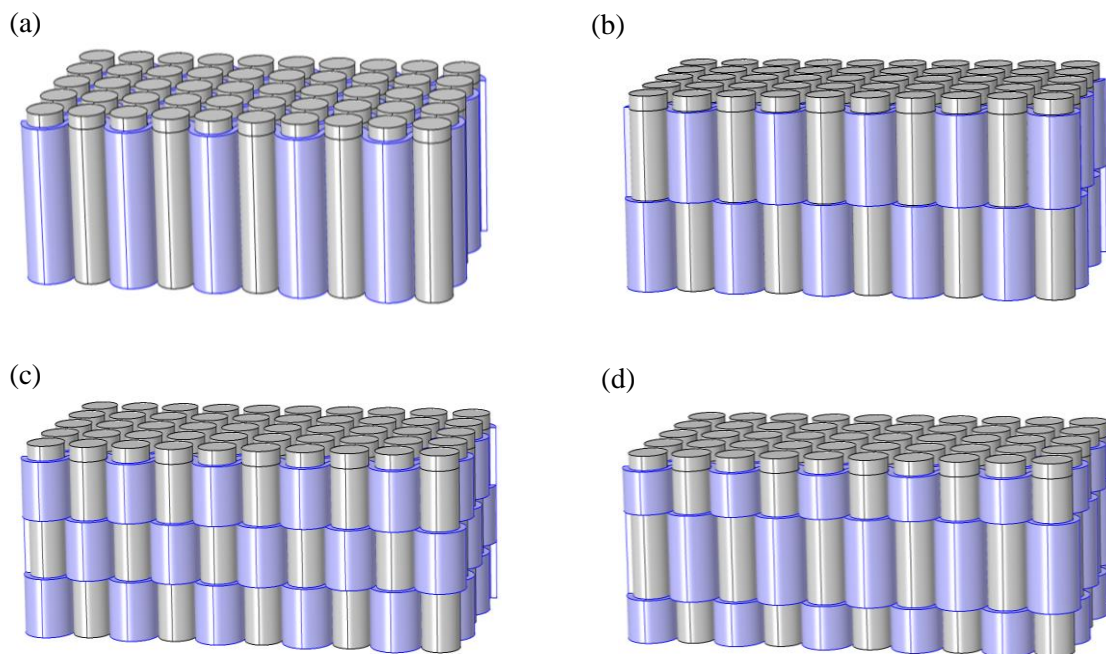


Figure 11. (a) Design 1 with one channel, (b) Design 2 with two channels, (c) Design 3 with three channels have the same height and (d) Design 4 with the height of the middle channel being twice that of the upper and lower channels.

Table 4. Maximum temperature and temperature difference of four designs

	Design 1	Design 2	Design 3	Design 4
T_{max}	305.03 K	303.96 K	303.77 K	303.61 K
ΔT_{max}	6.75 K	5.79 K	5.48 K	5.31 K

4. CONCLUSION

In this paper, a three-dimensional electrochemical-thermal fully coupled model of LIBs including a spiral wound structure is constructed. The precise temperature distribution and transient heat generation rate inside the battery are obtained. Then, a semi-enclosed S-shaped surrounding structure is proposed to dissipate the heat of the battery module. The effects of cooling channel height, width and inlet velocity on the heat dissipation performance are systematically discussed. Finally, by optimizing

the geometric structure of the liquid cooling channel, the heat dissipation efficiency of the module is effectively improved. The conclusions are as follows:

1. The height of the liquid cooling channel is not “the higher the better”, and it should be close to the height of the active material of the LIB. When the height of the liquid cooling channel reaches 60 mm, a further increase in the height has little effect on the heat dissipation of the battery. Therefore, the channel height is chosen to be 60 mm.

2. When choosing the width of the liquid cooling channel, the space utilization and cooling performance of the liquid-cooling device should be taken into account. Therefore, the channel width is set as 3 mm.

3. The influence of inlet velocity on the cooling performance of the module is very important. When the inlet velocity is more than 0.15 m/s, the maximum temperature of the battery during the entire discharge process can be lower than 303 K, and the maximum temperature difference is kept within 5 K.

4. Considering the difference between the axial and radial thermal conductivity of the battery, using multiple cooling channels in the vertical direction can disperse the heat dissipation area of the battery surface without directly increasing the contact area. This design effectively improves the heat dissipation performance of the liquid cooling system and significantly reduces the maximum temperature of the battery at the edge of the module.

ACKNOWLEDGMENTS

This work was supported by the Special Funds for the Transformation Program of Scientific and Technological Achievements of Jiangsu Province (BA2016162) and the Key Research and Development Program of Jiangsu Province (BE2019010).

References

1. S. Panchal, I. Dincer, M. Agelin-Chaab, R. Fraser, M. Fowler, *Int. J. Heat Mass Transfer*, 101 (2016) 1093.
2. H.L. Zhang, H.B. Zhao, M.A. Khan, W.W. Zou, J.Q. Xu, L. Zhang, J.J. Zhang, *J. Mater. Chem.*, 6 (2018) 20564.
3. F. Schipper, D. Aurbach, *Russ. J. Electrochem.*, 52 (2016) 1229.
4. V. Etacheri, R. Marom, E. Ran, G. Salitra, D. Aurbach, *Energy Environ. Sci.*, 4 (2011) 3243.
5. H. Li, X. Wang, Y. Zhu, Y.-P. Wang, *Int. J. Electrochem. Sci.*, 15 (2020) 3807.
6. L. Chen, R. Xu, W. Rao, H. Li, Y.-P. Wang, T. Yang and H.-B. Jiang, *Int. J. Electrochem. Sci.*, 14 (2019) 4124.
7. A. Hofmann, N. Uhlmann, C. Ziebert, O. Wiegand, A. Schmidt, T. Hanemann, *Appl. Therm. Eng.*, 124 (2017) 539.
8. T.M. Bandhauer, S. Garimella, T.F. Fuller, *J. Electrochem. Soc.*, 158 (2011) R1.
9. W. Wu, W. Wu, S. Wang, *Int. J. Heat Mass Transfer*, 121 (2018) 967.
10. A. Greco, X. Jiang, D. Cao, *J. Power Sources*, 278 (2015) 50.
11. Z.J. An, L. Jia, L.T. Wei, C. Dang, Q. Peng, *Appl. Therm. Eng.*, 137 (2018) 792.
12. L.H. Saw, Y. Ye, A.A.O. Tay, W.T. Chong, S.H. Kuan, M.C. Yew, *Appl. Energy*, 177 (2016) 783.
13. P. Nelson, D. Dees, K. Amine, G. Henriksen, *J. Power Sources*, 110 (2002) 349.
14. A.M. Sefidan, A. Sojoudi, S.C. Saha, *Int. J. Therm. Sci.*, 117 (2017) 44.
15. A. Greco, X. Jiang, D. Cao, *J. Power Sources*, 278 (2015) 50.

16. W. Wu, W. Wu, S. Wang, *Energy Convers. Manage.*, 153 (2017) 22.
17. S. Park, D.H. Jung, *J. Power Sources*, 227 (2013) 191.
18. Y. Wang, G.Q. Zhang, X.Q. Yang, *Appl. Therm. Eng.*, 162 (2019) 114200.
19. Y.X. Lai, W.X. Wu, K. Chen, S.F. Wang, C. Xin, *Int. J. Heat Mass Transfer*, 144 (2019) 118581.
20. C.R. Zhao, A.C.M. Sousa, F.M. Jiang, *Int. J. Heat Mass Transfer*, 129 (2019) 660.
21. Z.H. Rao, Z. Qian, Y. Kuang, Y.M. Li, *Appl. Therm. Eng.*, 123 (2017) 1514.
22. H.B. Zhou, F. Zhou, Q. Zhang, Q.Z. Wang, Z.B. Song, *Appl. Therm. Eng.*, 162 (2019) 114257.
23. N.X. Yang, X.W. Zhang, G.J. Li, D. Hua, *Appl. Therm. Eng.*, 80 (2015) 55.
24. K. Somasundarama, E. Birgerssonb, A.S. Mujumbara, *J. Power Sources*, 203 (2012) 84.
25. J. Chiew, C.S. Chin, W.D. Toh, Z. Gao, J. Jia, C.Z. Zhang, *Therm. Eng.*, 147 (2019) 450.
26. Y.H. Ye, Y.X. Shi, L.H. Saw, *Electrochim. Acta*, 121 (2014) 143.
27. Y.T. Huo, Z.H. Rao, X.J. Liu, J.T. Zhao, *Energy Convers. Manage.*, 89 (2015) 387.
28. K. Kumaresan, G. Sikha, R.E. White, *J. Electrochem. Soc.*, 155 (2008) A164.
29. S. Panchal, M. Mathew, R. Fraser, M. Fowler, *Therm. Eng.*, 135 (2018) 123.
30. A. Jarrett, I.Y. Kim, *J. Power Sources*, 245 (2014) 644.
31. W.F. Fang, O.J. Kwon, C.Y. Wang, *Int. J. Energy Res.*, 34 (2010) 107.
32. D.H. Jeon, S.M. Baek, *Energy Convers. Manage.*, 52 (2011) 2973.
33. Z. Qian, Y. Li, Z. Rao, *Energy Convers. Manage.*, 126 (2016) 622.
34. Y.T. Huo, Z.H. Rao, X.J. Liu, J.T. Zhao, *Energy Convers. Manage.*, 89 (2015) 387.
35. C. Zhao, W. Cao, *Int. J. Heat Mass Transfer*, 120 (2018) 751.
36. T.S. Zhang, Q. Gao, G.H. Wang, Y.L. Gu, *Appl. Therm. Eng.*, 116 (2017) 655.
37. W. Tong, K. Somasundaram, E. Birgersson, *Int. J. Therm. Sci.*, 94 (2015) 259.
38. J.T. Zhao, Z.H. Rao, Y.M. Li, *Energy Convers. Manage.*, 103 (2015) 157.